Self-assembly of the general membrane-remodeling protein PVAP into sevenfold virus-associated pyramids

Bertram Daum, Tessa E. F. Quax, Martin Sachse, Deryck J. Mills, Julia Reimann, Özkan Yildiz, Sabine Häder, Cosmin Saveanu, Patrick Forterre, Sonja-Verena Albers, et al.

Self-assembly of the general membrane-remodeling protein PVAP into 7-fold virus-associated pyramids

Bertram Daum [a,1], Tessa E.F. Quax [b,1], Martin Sachse[c], Deryck Mills[a], Julia Reimann[d], Özkan Yildiz[a], Sabine Häder[a], Cosmin Saveanu[e], Patrick Forterre [b], Sonja-Verena Albers[d], Werner Kühlbrandt[a,2] and David Prangishvili[b,2]

[a]Department of Structural Biology, Max Planck Institute of Biophysics, 60438 Frankfurt am Main, Germany

[b]Institut Pasteur, Biologie Moléculaire du Gène chez les Extrêmophiles, 75015 Paris, France

[c]Institut Pasteur, Plate-Forme de Microscopie Ultrastructurale, 75015 Paris, France.

[d]Molecular Biology of Archaea, Max-Planck Institute for Terrestrial Microbiology, 35043 Marburg, Germany

[e] Institut Pasteur, Génétique des Interactions Macromoléculaires , 75015 Paris, France

[1] These authors contributed equally to this work.

[2]to whom correspondence should be addressed.

(david.prangishvili@pasteur.fr, werner.kuehlbrandt@biophys.mpg.de)

Key words: archaea, virus, viral egress

Abstract

Viruses have developed a wide range of strategies to escape from host cells in which they replicate. Some archaeal viruses employ for egress a pyramidal structure with sevenfold rotational symmetry. Virus-associated pyramids (VAPs) assemble in the host cell membrane from the virus-encoded protein PVAP, and open at the end of the infection cycle. We characterize this unusual supramolecular assembly using a combination of genetic, biochemical and electron microscopic techniques. By whole-cell electron cryo-tomography, we monitor morphological changes in virus-infected host cells. Subtomogram averaging reveals the VAP structure. By heterologous expression of *PVAP* in cells from all three domains of life we demonstrate that the protein integrates indiscriminately into virtually any biological membrane, where it forms sevenfold pyramids. We identify the protein domains essential for VAP formation in PVAP truncation mutants by their ability to remodel the cell membrane. Self-assembly of PVAP into pyramids requires at least two different, in-plane and out-of-plane, protein interactions. Our findings allow us to propose a model of how PVAP arranges to form sevenfold pyramids and suggest how this small, robust protein may be used as a general membrane remodeling system.

Significance statement

The archeaovirus SIRV2 has developed unique mechanisms to penetrate the plasma membrane and S-layer of its host *Sulfolobus islandicus* to leave the cell after replication. SIRV2 encodes 10kDa protein PVAP, which assembles into 7-fold symmetric virus-associated pyramids (VAPs) in the host cell plasma membrane. Towards the end of the viral replication cycle, these VAPs open to form pores through the plasma membrane and S-layer, allowing viral egress. Here we show that PVAP inserts spontaneously and forms VAPs in any kind of biological membranes. By electron cryo-tomography we have obtained a 3D map of the VAP and present a model describing the assembly of PVAP into VAPs. Our findings open new avenues for a large variety of biotechnological applications.

\body

Introduction

Release of virus particles from infected cells is the last essential step of the viral replication cycle. In the course of this process, virions face the challenging task of crossing the cell envelope. Viruses have developed an arsenal of diverse strategies to overcome this problem. Most bacterial viruses are lytic and induce lysis of the infected cell with help of the holin-endolysin system (1), while others disrupt the host cell envelope via inhibition of the murein biosynthesis pathway (2). The morphological and genomic properties of archaeal viruses (3) suggested that their egress from host cells may have unusual traits that are different from those of bacterial viruses. Indeed, while most archaeal viruses exit cells without lysis, some, in particular the rod-shaped or icosahedral viruses that respectively infect *Sulfolobus islandicus* (SIRV2) and *Sulfolobus* turreted icosahedral virus 1 (STIV1), are lytic and exploit a special mechanism of virion egress (4-8). During the infection cycle of these viruses, pyramidal protrusions with sevenfold rotational symmetry form in the host cell membrane. As the final step of the infection cycle the VAPs open outwards along the seams of their seven facets, creating ~100 nm apertures through which the newly formed virions escape from the host cell (4, 7). VAPs consist of multiple copies of a ~10 kDa virus-encoded protein, which we term PVAP (SIRV2_P98) (7-9). Surprisingly, PVAP assembles into membrane pyramids even when expressed heterologously in archaeal and bacterial expression systems, demonstrating that no other viral proteins are required for VAP formation (7). The mechanism by which VAPs self-assembles in the membrane remains unknown.

In the present study we used electron cryo-tomography to investigate morphological features of SIRV2 replication and the formation of VAPs at different time points after infection. By subtomogram averaging, we determined a first 3D map of the VAP. This map, in combination with secondary structure predictions of PVAP and expression of *wild type PVAP* or a variety of truncation mutants in archaeal, bacterial and eukaryotic cells allows us to propose a model of how PVAP arranges to form the sevenfold pyramids. These insights are fundamental for understanding how this mechanism can be exploited as a universal tool to engineer the formation and controlled opening of large pores in biological or artificial lipid bilayers.

Results

SIRV2 induces morphological changes of the host cell

We analyzed morphological changes in *S. islandicus* during SIRV2 infection and the time points of VAP formation and opening by whole cell electron cryo-tomography at 0.5, 3, 6 and 12 hours post infection (h.p.i.). This allowed us to monitor morphological changes at high resolution and to compare these with previous results obtained by thin-sectioning of chemically fixed cells during the final stages of SIRV2 infection (4). Up to 3 h.p.i. infected cells were indistinguishable from uninfected control cells and no virions were visible in the cytoplasm (Figs. 1*a*). This suggests that SIRV2 does not enter the cell as an intact virus particle, in accordance with a previous study, in which we have directly observed infection of *S. islandicus* by SIRV2 in the electron microscope (10). Electron-dense ~100 nm globules were the only conspicuous features in the cytoplasm of controls and infected cells (Fig.1*a*), similar to those reported for *S. solfataricus* cells (11). However, each cell, infected or not, contained one or a few of these globules, which are therefore unrelated to virus replication. Their size and density above the cytoplasmic background indicates that they may be storage granules (12).

At 3-6 h.p.i., about half way through the infection cycle, newly assembled virions became visible in the cytoplasm as described earlier (4). They were organized in up to three bundles per cell, each consisting of roughly 50 rod-shaped particles (Fig.1*b*). Starting from 3 h.p.i., VAPs of various sizes formed in the plasma membrane of the host cells, most of which had penetrated the S-layer (Fig. 1*b*, 2 *a-d*). Each cell contained on average about 10 VAPs. The height of the VAPs (measured from the membrane to the tip of the pyramid) ranged from ~20nm to 150nm. At an early stage of formation, the VAPs in the plasma membrane had not yet punctured the S-layer of the host cell (Supplementary Fig. 1), but they already had the distinct features of hollow heptagonal pyramids, corroborating the earlier assumption that VAPs grow from the base by gradual expansion of their triangular facets (7). Very occasionally, VAPs contained a spherical storage granule (Fig. 2c). These granules likely correspond to the previously described intra-pyramidal bodies (IPB) in STIV-induced VAPs (11). Analysis of cells at distinct time points post infection showed that at 6 h.p.i. a number of VAPs had opened. The fraction of open VAPs increased, until at 12 h.p.i. all VAPs had unfolded, like the petals of a flower (Fig. 1*c,* 2*e-h*). The VAPs appeared to open as the pyramidal structures broke along the seams of the triangular pyramid faces (Fig. 2*f*). The VAP facets curved outwards with counter-clockwise handedness when viewed from the cell exterior (Fig. 2*f*), as suggested by electron micrographs of isolated VAPs (7). As the VAPs opened, the virion bundles disintegrated and individual virions diffused into the medium through the open VAPs (Fig. 3).

VAP structure

The shape of isolated VAPs has previously been investigated by negative staining and electron microscopy (7). To gain insight in the structure of VAPs *in situ,* closed or open VAPs were imaged by whole-cell electron cryo-tomography (Fig. 4*a*-*c*). The triangular faces of all VAPs appeared to consist of two distinct layers, irrespective of their conformation or stage of assembly. The ~4.5±1 nm outer layer was continuous with, and indistinguishable from, the cell membrane. The inner layer had a thickness of ~4.0±1 nm (Fig. 4). The centre-to-centre distance between the two layers was 10.0±1 nm, leaving a 5.8±1 nm gap of lower density. At the base of each VAP, the inner layer extended up to 15 nm beyond the outer layer into the cytoplasm. This suggests that the inner layer consists of a protein sheet that is attached and runs parallel to the cytoplasmic membrane surface (Fig. 4).

In order to verify that both layers of the VAP consist only of PVAP protomers, we analysed archaeal (*S. acidocaldarius*) or bacterial (*E. coli*) *PVAP* expression mutants constructed in a previous study (7). Whole-cell electron cryo-tomography of transformed cells revealed the distinctive two layers in all VAPs (Fig. 4c, S3), indicating that both consist solely of PVAP (Supplementary Fig. 3).

Subtomogram averaging of VAPs

A 3D map of the VAP was obtained by averaging 57 tomographic subvolumes of closed VAPs in the membrane of *PVAP*-expressing *E. coli* cells. Sections through the averaged volume parallel to the membrane showed clear sevenfold symmetry (Supplementary Fig. 4), which was applied to the final average to further improve the signal-to-noise ratio (Fig. 4*d*-*k*, Supplementary movie 1). The local resolution estimated by the program ResMap (13) was between 36 and 58 Å, with a mean resolution of ~43Å (Supplementary Fig. 5). Since VAPs come in different sizes, only the upper parts of the pyramids, to a height of ~62 nm and an outer diameter of ~96 nm, were used for averaging. At the tip, the inner opening angle of the pyramid was ~80° (Fig. 4*d*). As observed in the raw tomograms, the structure consisted of two layers (Fig. 4*d*, *e*, *i*-*k*). The outer layer formed a continuous envelope, consisting of seven triangular facets (Fig. 4*f*-*k*). As seen from the outside, the facets had a perceptible counter-clockwise handedness (Fig. 4*f*) and each facet was slightly convex towards the inside (Fig. 4*f, g, j, k*). The angle at the tip of the triangular facets was 35°, in accordance with previous measurements on isolated VAP fragments (7). Overall, the entire structure had the appearance of a tent or teepee (Fig. 4 *g).* The inner, cytosolic layer of the pyramid consisted of seven triangular sheets parallel to the membrane on the outside (Fig. 4*i*-*k*). Cross-sections through the sevenfold averaged volume revealed narrow connecting densities between the two layers of the pyramid, suggesting that they are physically linked (Fig. 4*k*).

Membrane remodelling by PVAP

In silico secondary structure predictions (14) and hydrophobicity analysis (15) of PVAP suggest that the protein consists of an N-terminal transmembrane helix (residues 5-34), followed by three hydrophilic α-helices of two to three turns each, separated by short linker regions (Supplementary Fig. 2). The PSORT-server (16) indicated that PVAP does not contain a pre-sequence. This is consistent with a previous study of the N-terminal amino acid sequence of purified PVAP of SIRV2 with Edman degradation, which did not indicate a cleavable signal sequence (9). Thus, we assumed that the hydrophobicity of its predicted N-terminal transmembrane segment drives the spontaneous insertion of PVAP into the lipid bilayer. To test this hypothesis, *PVAP* was expressed in the *Saccharomyces cerevisiae*, an eukaryotic organism. Cells were harvested 16 hours after induction of *PVAP* expression, high-pressure frozen and freeze-substituted. In addition, sections prepared by the Tokuyasu method (17) were immunolabeled with antibodies raised against PVAP. All samples were analysed by transmission electron microscopy. Surprisingly, VAPs were found in most, if not all, cellular membranes. In terms of size and appearance, the pyramids were indistinguishable from those that assembled in *E.coli* after PVAP expression or in *S. islandicus* after SIRV2 infection. PVAP-specific antibodies labeled VAPs in the nuclear envelope, the endoplasmic reticulum, Golgi apparatus, intracellular vesicles and mitochondria (Fig. 5).

Role of PVAP domains in VAP assembly

To identify which parts of the PVAP are required for VAP assembly, truncated mutants lacking the last 10, 20, 30, 40 or 70 C-terminal residues (*ΔC10, ΔC20, ΔC30, ΔC40* or *ΔC70*) were constructed (Fig. 6). EM analysis of *E.coli* cells transfected with these constructs revealed VAPs only in case of the *ΔC10* mutant (Fig. 6*).*

By contrast, VAPs did not form after truncation of 20 to 70 C-terminal residues (PVAP*ΔC20, ΔC30, ΔC40 or ΔC70*, Fig. 6), corresponding to one to three C-terminal α-helical segments. Instead, expression of these constructs resulted mostly in protein aggregates. In addition, constructs lacking 20-40 C-terminal residues caused the inner membrane of *E.coli* to form large invaginations, suggesting that these variants still interact with the membrane (Fig 6*b*). The effect was most pronounced for PVAPΔC20. In contrast, PVAPΔC70 did not produce any membrane invaginations (Fig 6*b*).

Expression of a *PVAP* construct lacking the predicted N-terminal transmembrane helix (*PVAPΔN30*) likewise did not result in VAP formation. There was no sign of any interaction with

the membrane (Fig. 6*b*), indicating that the N-terminal transmembrane domain is indeed required for membrane insertion of PVAP protomers.

We asked if the PVAP transmembrane domain is essential for VAP formation or could be replaced by any other transmembrane domain. To characterize the role of the PVAP transmembrane domain in VAP formation we constructed a chimera by fusing the *E. coli* flagellar regulator *Flk*, a gene encoding a single trans-membrane helix inner membrane protein (18) to *PVAPΔN30*, replacing the N-terminal transmembrane helix (residues 1-30) of PVAP(18). After expression, this fusion construct (PVAPtmFlk) was indeed inserted into the membrane, as judged by Western blot analysis of cell fractions with SIRV2-PVAP antibody (Supplementary Fig. 6). However, there was no evidence of VAPs in these cells (Fig 6*b*).

Taken together these findings indicate that the N-terminal domain is essential for membrane insertion of PVAP and for the interaction between PVAP protomers, which results in the assembly of a protein sheet on the inner membrane surface. The C-terminal domain of PVAP (except the last 10 residues, which are predicted to be disordered) is required for VAP formation. Without this domain, the protein aggregates instead of forming VAPs.

PVAP oligomers

To characterize the oligomerization of PVAP *in vitro*, we fused a His-tag to the C-terminus and expressed the protein heterologously in *E. coli*. Isolated membranes were solubilized with the detergent N-laurylsarcosine. PVAP was purified by nickel affinity chromatography and size exclusion chromatography. The single peak in the gel filtration profile corresponds to a molecular mass of ~70 kDa (Supplementary Fig. 7). SDS-PAGE analysis of peak fractions show discrete PVAP bands at ~10, 20, 30 and 70 kDa (Supplementary Fig. 7), indicating that in detergent solution PVAP forms different oligomers, the largest of which is most likely a heptamer. A PVAP heptamer is also suggested by gel filtration chromatography.

Discussion

The VAP, an archeoviral egress structure that takes the shape of a large sevenfold pyramid in the host membrane, is without parallel in biology. It consists of multiple copies of PVAP, a 10 kDa membrane protein, which forms VAPs in the membrane, evidently without the need for any other cellular component.

How does the 10 kDa PVAP assemble to form sevenfold pyramids in the membrane? To address this question, we investigated the VAP structure itself by electron cryo-tomography, and have

studied the membrane insertion and biochemical properties of PVAP. We have demonstrated that PVAP forms VAPs in archaeal, bacterial and eukaryotic membranes, into which it inserts indiscriminately, and that, with the exception of the last 10 C-terminal residues, the entire length of the protein is required for VAP assembly. Finally, we have shown that PVAP forms oligomers, most likely heptamers, in detergent solution.

PVAP is a universal membrane remodeling system

Sequence analysis of PVAP suggested that the protein does not contain a signal sequence and thus most likely integrates spontaneously into the archaeal membrane. A similar mechanism of membrane insertion has been found for tail-anchored (TA) proteins (19) and for bacterial pore-forming toxins (bPTFs) (20). TA proteins are indigenous proteins, which contain a single C-terminal transmembrane segment. They are inserted into their target membrane in a Sec-independent, but organelle-specific manner, occasionally aided by cytoplasmic chaperones (19). Similar to PVAP, bPTFs are expressed as monomers and insert into the target membrane, where they assemble into pore-forming oligomers, either to kill other bacteria or, in case of pathogens, to lyse the host membrane and thus to aid bacterial proliferation (20).

Overexpression of *PVAP* in the archaeon *S. acidocaldarius*, the bacterium *E. coli* and the eukaryote *S. cerevisiae* resulted in the formation of VAPs in the plasma membranes of all hosts. Even more remarkably, VAPs were observed in virtually all cellular membranes of the eukaryote *S. cerevisiae*, including the nuclear envelope, the ER, the mitochondrial outer membrane and the plasma membrane. This demonstrates that, in contrast to other known type of protein spontaneously integrating into membranes, PVAP is able to insert into practically any biological lipid bilayer, solely by virtue of its N-terminal transmembrane segment. Once inserted into the bilayer, it forms sevenfold pyramids, irrespective of fundamental differences in lipid or protein composition of the target membrane. These characteristics render PVAP a unique, universal membrane remodeling tool.

Supramolecular organisation of VAPs

Whole-cell electron cryo-tomography and subtomogram averaging revealed that the VAPs consist of the same two layers of roughly equal thickness in all endogenous and heterologous expression hosts. The outer layer was continuous with the plasma membrane, whereas the inner layer formed a discontinuous sheet at the cytoplasmic membrane surface. As PVAP must insert with its N-terminal TM segment into the plasma membrane, the outer layer most likely consists of multiple copies of this part of PVAP plus interspersed membrane lipid. In turn, the cytoplasmic protein sheet must consist of the tightly associated C-terminal domains of the

protein. The low-density region between the two layers would then account for the linker region between the cytoplasmic domains and the N-terminal trans-membrane segments (Fig. 7a).

Recently it was suggested that the opening of STIV-induced VAPs depends on polymerization of ESCRT-III homologs, resulting in the 'stripping' of VAPs from their cytoplasmic membrane (21). Our observation that the outer layer of the double-layered VAP structure is continuous with the plasma membrane (Fig 4) does not support this model. Moreover, global analysis of host gene expression during the SIRV2 infection cycle documented that ESCRT-III-like proteins were down-regulated in infected cells (22). Thus, it is possible, although not very likely, that mechanisms of VAP opening differ in SIRV2-infected and STIV-infected cells.

Our tomograms of closed and open VAPs throw some light on the mechanism by which the pyramids open to facilitate viral egress. The seven edges of the closed pyramid are slightly curved in a right-handed fashion (Fig. 4 f). In the open state, the edges of the seven individual facets are curved in the same way (Fig. 4 f). In the open VAP, each facet curls outwards (Fig. 4 f). This suggests that in the closed state, the VAP structure is under mechanical tension. This tension is likely to provide the energy required for VAP opening. As the tip of the VAP displays the point of strongest membrane curvature in the whole assembly, it most likely serves as predetermined breaking point, at which the pyramid would begin to unfold along its seams.

VAP assembly and opening

We propose a model for VAP assembly (Fig. 7). Upon synthesis in the cytosol, PVAP integrates spontaneously into the cell membrane, depending solely on the hydrophobicity of its N-terminal transmembrane helix segment. In the membrane, tight interactions between PVAP protomers result in the formation of protein sheets, which consist of the observed two layers. We propose that this interaction involves both the N-terminal transmembrane helices and the C-terminal hydrophilic PVAP domains, as indicated by the expression of truncation constructs.

In order to assemble into a pyramid instead of a flat sheet, at least two different kinds of interactions between PVAPs are necessary, one in-plane interaction within the triangular facets, and one out-of-plane interaction, at the edges of the pyramid. The interaction at the edges is most likely weaker than the in-plane interaction, so that the pyramids open along these lines. Since all VAPs observed in *S. islandicus* or in heterologous systems grow to roughly the same size, the expansion of VAP must be constrained in some way.

At present it is unknown if the pyramids are built in a one-by-one self-assembly process from individual PVAP protomers or if, upon membrane insertion, the protomers assemble into heptamers, which then combine into pyramids in a second stage of assembly. The prior formation of heptamers in the membrane is suggested by the gel filtration experiments, which show one homogenous peak of ~70 kDa in detergent solution. Given that detergent mimics the hydrophobic membrane environment, it is not unlikely that the same interactions that give rise to the heptamer in a detergent micelle would also promote the formation of heptamers in the membrane, which may thus be the building blocks of the pyramids.

VAP opening presumably involves a host or virus-specific factor, since the pyramids only open in virus-infected *Sulfolobus* cells but remain closed in PVAP-expressing bacteria and yeast. Once the mechanism that triggers VAP opening is elucidated, this system could be utilised to introduce ~100 nm apertures in any lipid bilayer. VAPs might then be used for targeted drug delivery, releasing compounds from liposomes upon a specific signal. In addition, the PVAP transmembrane domain has the ability to insert into all types of biological membranes and may therefore be fused to proteins that otherwise cannot be reconstituted into lipid bilayers. This system thus has interesting potential applications in basic research, biotechnology and therapy.

Materials and Methods

Virus and host strains *S. islandicus* LAL 14/1 cells were grown, synchronized and infected with SIRV2 as described previously (7) and in the Supplementary Information (SI).

Plasmid constructs and transformation of *S. acidocaldarius* SIRV2_ORF98 (NCBI RefSeq ID: NP_666583) was amplified from SIRV2 genomic DNA and cloned into the pSVA1450 plasmid behind an araS promoter, which yielded pTQ26. pTQ26 was transformed to *S. acidocaldarius* M31 as described in the SI.

Plasmid constructs and transformation of *E.coli* SIRV2_ORF98 was amplified from SIRV2 genomic DNA with different primers resulting in 3' truncated PCR products of 267, 237, 207, 177 and 87 bp. A 5' truncation of ORF98 was created by amplification of a 216 bp product starting at position 81. The same sequence was fused with the 75 bp transmembrane segment of the *E.coli Flk* gene as described in the SI. All *PVAP* gene mutants were cloned into the T7 promoter–driven expression vector pSA4. Expression was induced with isopropyl β-d-1-thiogalactopyranoside (IPTG). Analysis of *PVAP* expressing cultures by high pressure freezing, freeze substitution and western blotting was performed as described in ref (9) and (7).

Plasmid constructs and transformation of *S. cerevisiae* *SIRV2_ORF98* was amplified from SIRV2 genomic DNA and cloned in the expression vector pCM190. *S. cerivisiae* was transformed with this plasmid. A pre-culture was grown in selective medium as described in the SI. After one day, cells were diluted 1/1000 in medium without doxycyclin.

Immuno-electron microscopy Yeast cells were fixed, washed, pelleted in gelatin and the gelatine pellet was solidifed on ice and cut into small blocks as described in the SI. These were infiltrated 2.3M sucrose, mounted on aluminium pins and frozen in liquid nitrogen. Thin sections were cut and picked up in a 1:1 mixture of 2.3M sucrose and 2% methylcellulose. Labelling for PVAP was done as described previously (7).

High-pressure freezing and freeze-substitution *E.coli* cells were taken up in cellulose capillary tubes and *S. cerevisiae* cultures were concentrated by filtration. Samples were high-pressure frozen and freeze-substitution was performed in anhydrous acetone containing 2% osmium tetroxide. Afterwards the samples were washed with dry acetone and embedded stepwise in EPON. After heat polymerization thin sections were cut, collected on 200 mesh

Formvar-coated copper grids and post-stained as described in the SI. Images were recorded with a JEOL 1010 electron microscope equipped with an Olympus Keen View camera.

Whole cell cryo-tomography *S. islandicus* cells were harvested, concentrated by low-speed centrifugation and plunge-frozen. *E. coli* cells overexpressing *PVAP* were harvested at the same conditions, washed once in 50mM Tris, 300mM NaCl, pH7 and plunge-frozen in the same buffer. Before freezing, suspensions were mixed with an equal volume of 10 nm colloidal protein-A gold suspension. Tomograms were recorded with a Polara G2 Tecnai field emission transmission electron microscope equipped with a Gatan Tridiem energy filter and 2x2 k CCD camera. Tomographic tilt series of zero-loss filtered images were recorded and tomograms reconstructed as described in the SI.

Subtomogram averaging For subtomogram averaging of VAPs, 57 pyramid volumes were cut out from a single tomogram of a PVAP overexpressing *E. coli* cell, aligned and averaged applying 7-fold rotational symmetry using the PEET software as described in the SI. The resolution of the map was estimated using the ResMap software (13).

PVAP purification A codon-optimized SIRV_ORF98 gene was synthetized and inserted in the plasmid pET26b. *E. coli* BL21DE3/Rosetta/pLysS cells were transformed with this plasmid. Protein expression was induced with 1mM IPTG. After 2 hours, cells were pelleted, resuspended in lysis buffer and disrupted with a Microfluidizer. The membrane fraction was pelleted by centrifugation, and diluted in 50 mM Tris pH 7.0, 300 mM NaCl to a protein concentration of 5 mg/ml. 1.5% N-laurylsarcosine was added. After high-speed centrifugation the supernatant was loaded onto a Ni-NTA column followed by several washing steps. The protein was eluted in buffer containing 500 mM imidazole and concentrated using Amicon spin columns with a 30 kDa cutoff prior to loading onto a gel filtration column, as described in more detail in the SI.

Acknowledgements

We thank John van der Oost and Alain Jacquier for helpful discussions and Alp Kuckelbir for help with ResMap. DP and TQ acknowledge financial support of L' Agence nationale de la recherche. WK and BD acknowledge financial support from the Max Planck Society.

Data deposition: The map and fitted model reported in this paper have been deposited in the Electron Microscopy Data Bank (accession no. 5844).

394

395

References

1. Krupovic M & Bamford DH (2008) Holin of bacteriophage lambda: structural insights into a membrane lesion. *Mol Microbiol* 69(4):781-783.
2. Bernhardt TG, Wang IN, Struck DK, & Young R (2002) Breaking free: "protein antibiotics" and phage lysis. *Res Microbiol* 153(8):493-501.
3. Prangishvili D (2013) The wonderful world of archaeal viruses. *Ann rev microbiol* 67:565-585.
4. Bize A*, et al.* (2009) A unique virus release mechanism in the Archaea. *Proc Natl Acad Sci U S A* 106(27):11306-11311.
5. Brumfield SK*, et al.* (2009) Particle assembly and ultrastructural features associated with replication of the lytic archaeal virus sulfolobus turreted icosahedral virus. *J Virol* 83(12):5964-5970.
6. Prangishvili D & Quax TE (2011) Exceptional virion release mechanism: one more surprise from archaeal viruses. *Curr Opin Microbiol* 14(3):315-320.
7. Quax TE*, et al.* (2011) Simple and elegant design of a virion egress structure in Archaea. *Proc Natl Acad Sci U S A* 108(8):3354-3359.
8. Snyder JC, Brumfield SK, Peng N, She Q, & Young MJ (2011) Sulfolobus turreted icosahedral virus c92 protein responsible for the formation of pyramid-like cellular lysis structures. *J Virol* 85(13):6287-6292.
9. Quax TE, Krupovic M, Lucas S, Forterre P, & Prangishvili D (2010) The Sulfolobus rod-shaped virus 2 encodes a prominent structural component of the unique virion release system in Archaea. *Virology* 404(1):1-4.
10. Quemin ER*, et al.* (2013) First insights into the entry process of hyperthermophilic archaeal viruses. *J Virol* 87(24):13379-13385.
11. Fu CY*, et al.* (2010) In vivo assembly of an archaeal virus studied with whole-cell electron cryotomography. *Structure* 18(12):1579-1586.
12. Iancu CV*, et al.* (2010) Organization, structure, and assembly of alpha-carboxysomes determined by electron cryotomography of intact cells. *J Mol Biol* 396(1):105-117.
13. Kucukelbir A, Sigworth FJ, & Tagare HD (2013) Quantifying the local resolution of cryo-EM density maps. *Nature meth*.
14. Sapay N, Guermeur Y, & Deleage G (2006) Prediction of amphipathic in-plane membrane anchors in monotopic proteins using a SVM classifier. *Bmc Bioinformatics* 7.
15. Krogh A, Larsson B, von Heijne G, & Sonnhammer EL (2001) Predicting transmembrane protein topology with a hidden Markov model: application to complete genomes. *J Mol Biol* 305(3):567-580.
16. Nakai K & Kanehisa M (1991) Expert system for predicting protein localization sites in gram-negative bacteria. *Proteins* 11(2):95-110.
17. Tokuyasu KT (1973) A technique for ultracryotomy of cell suspensions and tissues. *The J cell biol* 57(2):551-565.
18. Borgese N & Righi M (2010) Remote origins of tail-anchored proteins. *Traffic* 11(7):877-885.
19. Borgese N & Fasana E (2011) Targeting pathways of C-tail-anchored proteins. *Biochim Biophys Acta* 1808(3):937-946.
20. Bischofberger M, Iacovache I, & van der Goot FG (2012) Pathogenic pore-forming proteins: function and host response. *Cell host & microbe* 12(3):266-275.
21. Snyder JC, Samson RY, Brumfield SK, Bell SD, & Young MJ (2013) Functional interplay between a virus and the ESCRT machinery in archaea. *Proc Natl Acad Sci U S A* 110(26):10783-10787.
22. Quax TE*, et al.* (2013) Massive Activation of Archaeal Defense Genes during Viral Infection. *J Virol* 87(15):8419-8428.

Figure Legends

Fig. 1. Morphological changes of *S. islandicus* during infection with SIRV2. Tomographic slices of typical archaeal cells at 0.5 (a), 3-6 (b) and 9 (c) hours post infection with SIRV2. Black arrowheads, closed VAPs; white arrowheads, open VAPs. Scale bars, 500 nm.

Fig. 2. VAPs in closed and open conformation. (a, c, e, g) Tomographic slice and segmented, surface-rendered volumes (b, d, f, h) of VAPs in the membrane of SIRV2-infected *S. islandicus* cells. VAPs are either closed (a-d) or open (e-h). The S-layer is purple, the cell membrane blue and the VAP is yellow. Scale bars, 200nm

Fig. 3. SIRV2 virion egress. Rendered tomographic volume of a SIRV2-infected *S. islandicus* cell, 12 h post infection. SIRV2 virions (orange, brown, purple) are released through open VAPs (yellow) that create ~ 100 nm apertures in the plasma membrane and S-layer (green). Orange, virions inside the cell; purple, virions escaping from the cell; brown, virion outside the cell. Transparent blue, viral or host DNA. Scale bar: 500 nm.

Fig. 4. VAP structure. Tomographic slices through closed (a) and open (b) SIRV2-induced VAPs of *S.islandicus* and VAPs formed after PVAP expression in *E.coli* (c), indicating two layers, one of which is continuous with the cell membrane (black arrowheads), while the other (white arrowheads) forms a sheet at the cytoplasmic surface of the membrane. VAPs in *S. islandicus* protrude trough the S-layer (white arrows). (d-k) 3D map of VAP obtained by subtomogram averaging, with sevenfold symmetry applied. Tomographic slice perpendicular to the pyramid base (d) and successive tomographic slices parallel to the base (e) show the two layers in the walls of the pyramid. (f) Top-view of the 3D map in solid representation shows that the edges of the of the seven pyramidal facets are slightly curved counter-clockwise (dotted lines). (g-k) Different orientations of the 3D map in surface representation. Transparent mesh and golden surface show different threshold levels. Black and white arrowheads indicate outer and inner layer, respectively. Open arrowheads indicate connections between inner and outer layers of the VAP. Scale bars, 200 nm (a-c), 50 nm (d-k).

Fig. 5. VAP formation in *S. cerevisiae*. *PVAP* expression in *S. cerevisiae* causes VAP formation in various cellular membranes. (a,b) Immuno-labelling of unfrozen cryo-sections with anti-PVAP antibodies. (a) VAP in the endoplasmic reticulum. (b) VAPs in mitochondrial membranes (c)

Freeze-substituted cell with VAP in the nuclear envelope. The inset shows an enlarged VAP. P, plasma membrane; CW, cell wall; M, mitochondrion; N, nucleus. Arrows indicate VAPs. Scale bars, 200 nm.

Fig. 6. Expression of *PVAP* variants in *E.coli*. Several PVAP truncation mutants were constructed. (a) Schematic representation of PVAP constructs expressed in *E.coli*. (PVAP) wild type PVAP. (PVAP*ΔC10*) PVAP lacking 10, (PVAP*ΔC20*) 20, (PVAP*ΔC30*) 30, (PVAP*ΔC40*) 40, or (PVAP*ΔC70*) 70 C-terminal residues. (PVAP*tmFlk*) PVAP construct in which the transmembrane segment is replaced by that of the *E.coli* membrane protein Flk. (PVAP*ΔN30*) PVAP lacking the N-terminal transmembrane segment. (b) Electron micrographs of thin sections trough *E.coli* cells expressing PVAP constructs as in A. VAPs (open arrows) and invagination of the membrane (black arrow) are shown; Bars, 200 nm; bar in inset, 100 nm.

Fig. 7. Model of VAP assembly. (a) Predicted secondary structure of PVAP, with N-terminal trans-membrane helix and three short C-terminal α-helices. (b) Schematic top view of the VAP, with its seven facets in different colours. Strong interactions between individual PVAP protomers stabilise the integrity of each facet, whereas weak interactions at the seams (white dashed lines) between two neighbouring facets form predetermined break points. The black dashed indicates the cross section through the VAP in in c. (c) PVAP protomers (green) insert spontaneously into the plasma membrane (blue), with the short C-terminal helices exposed to the cytoplasm. Close contacts between PVAP molecules in each facet (aqua and orange outline) exclude S-layer proteins (grey), and combine into a protein sheet below the plasma membrane. Addition of PVAP units at the base pushes the pyramid outwards.

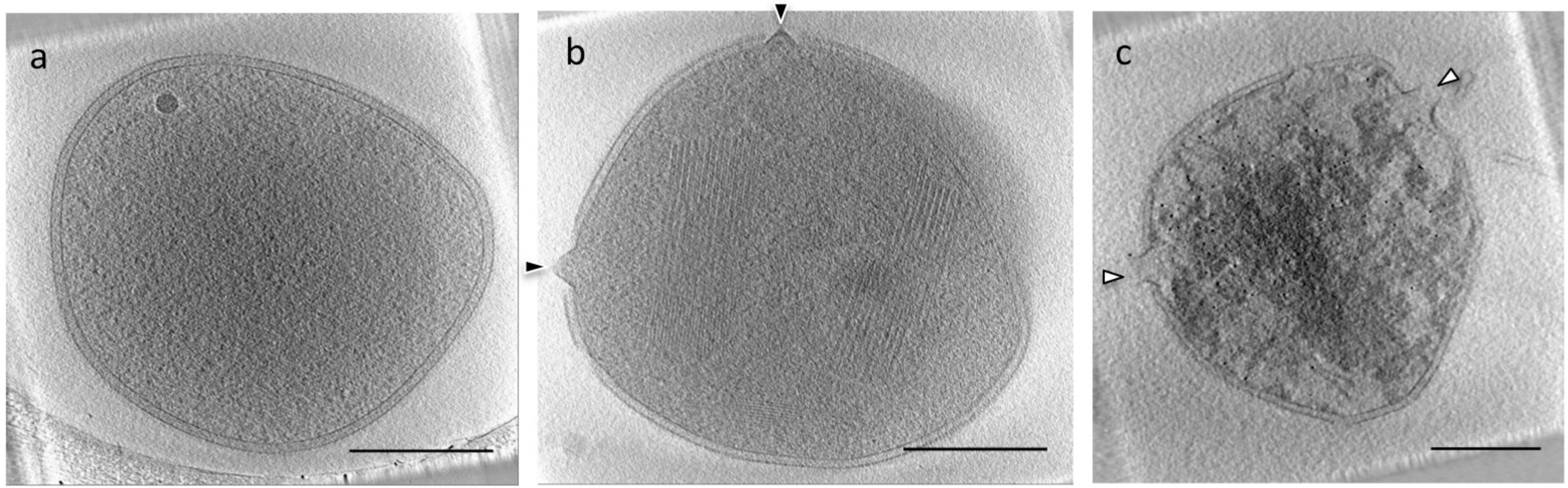
a
b
c

Figure 2

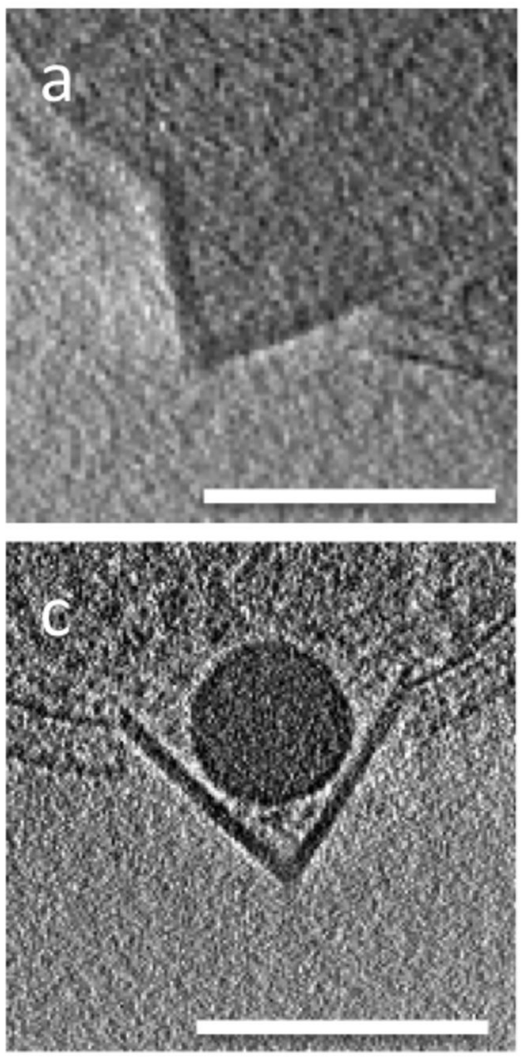

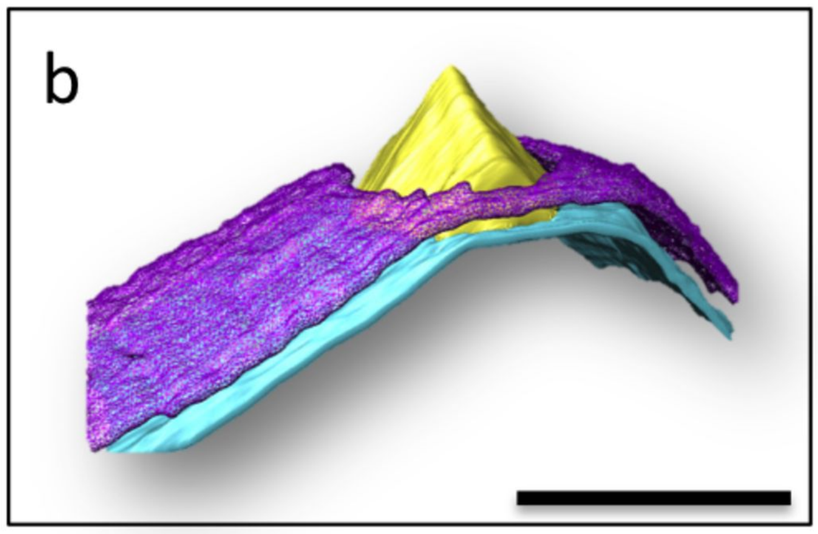

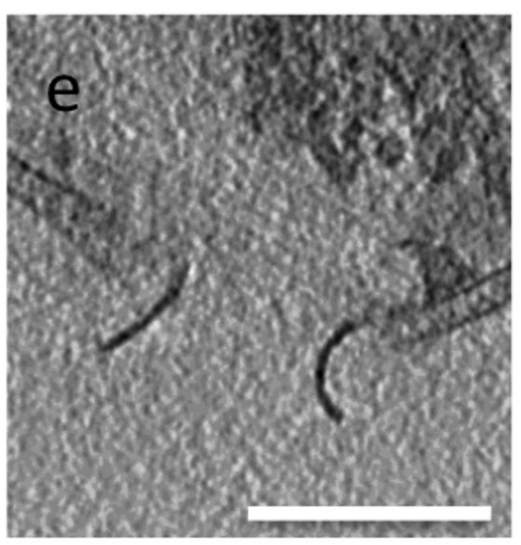

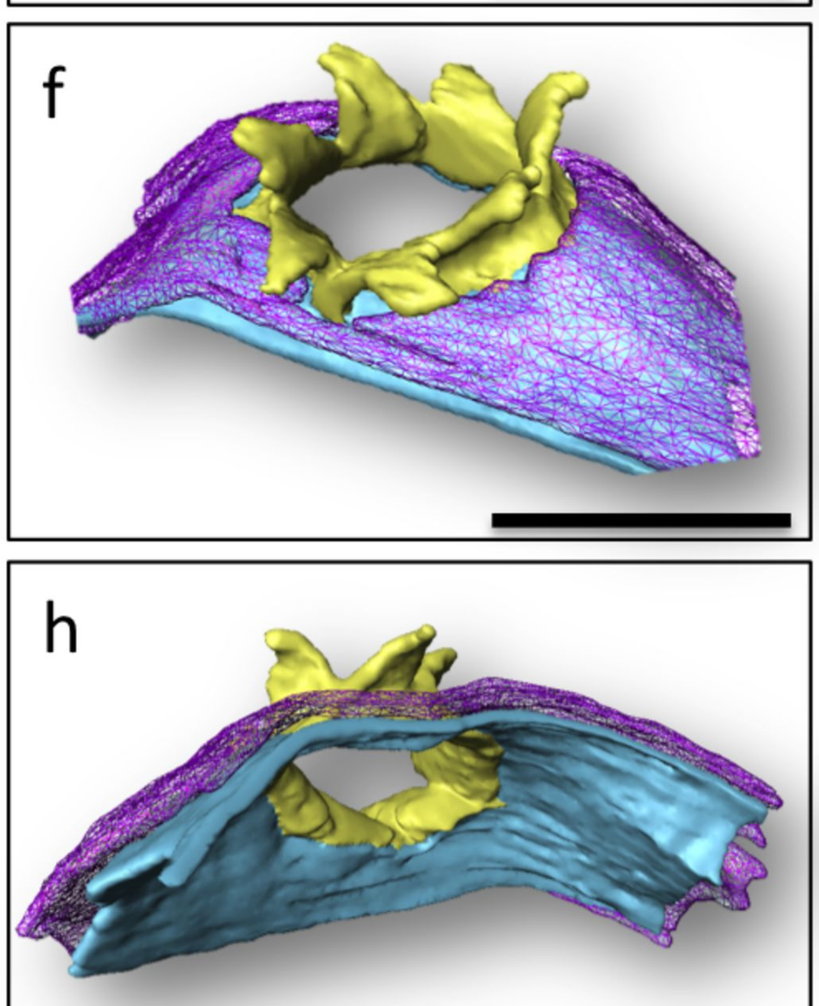

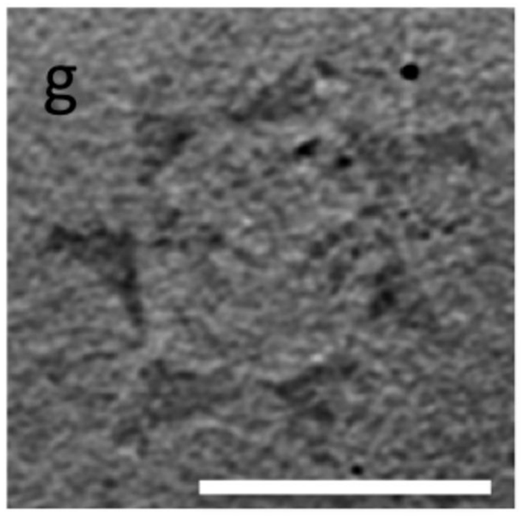

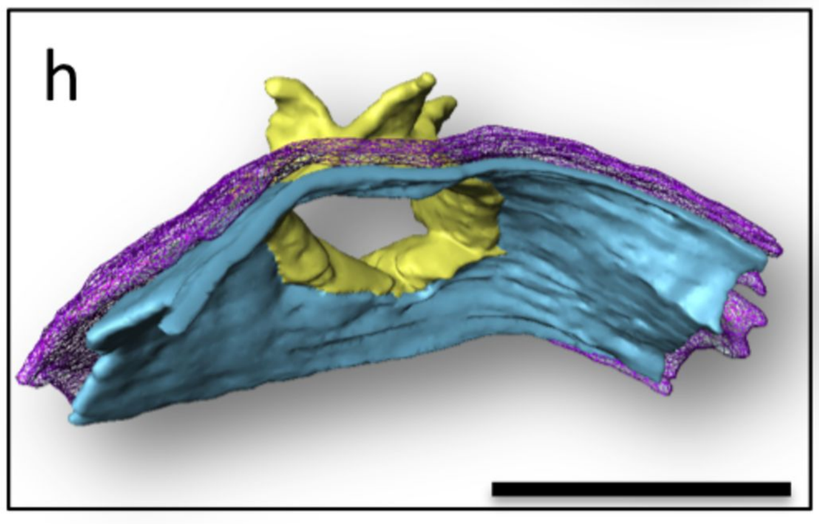

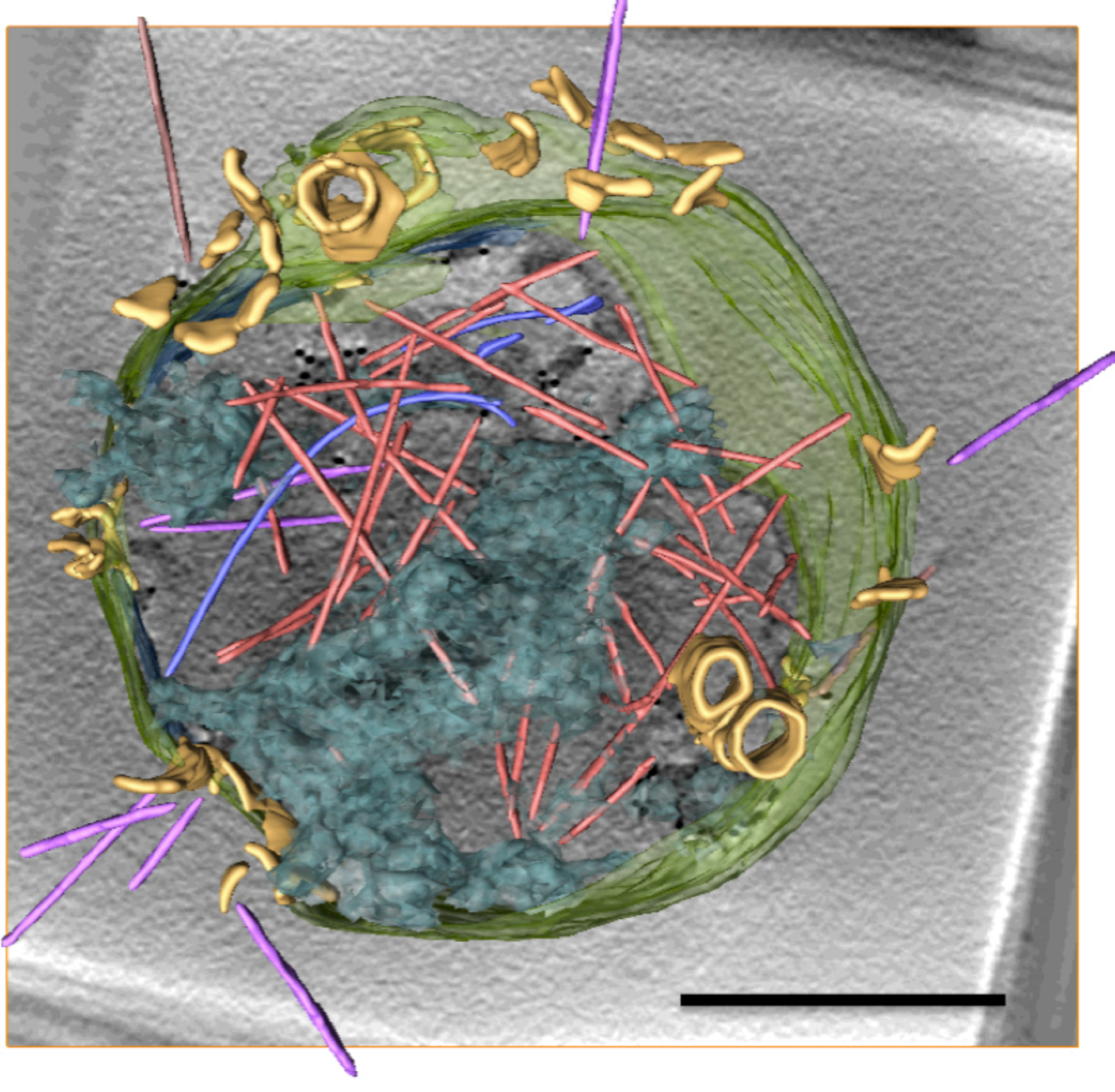

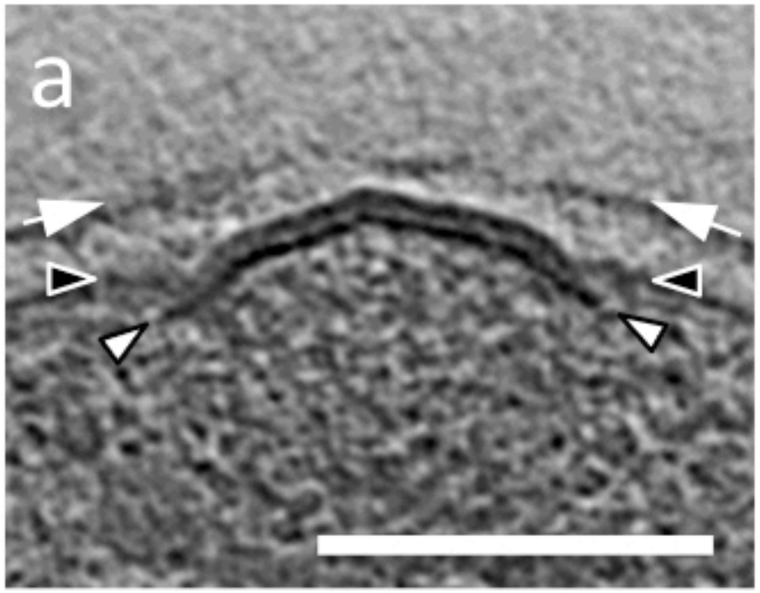
a

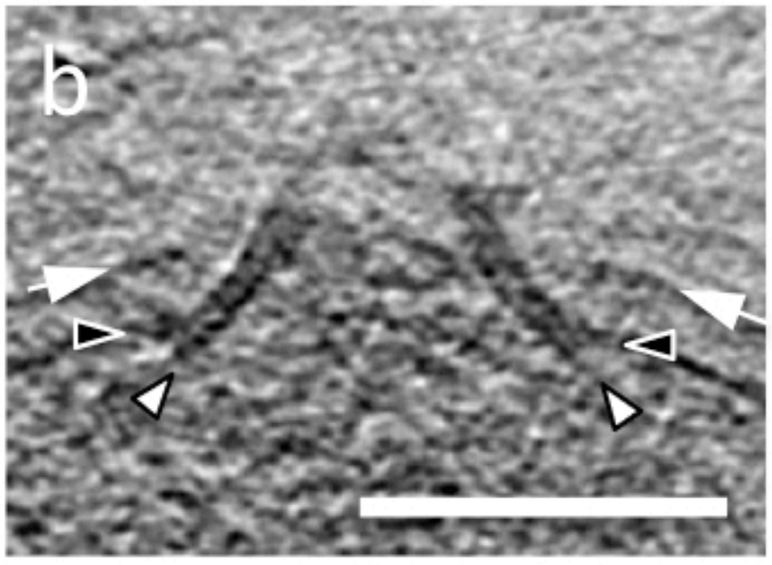
b

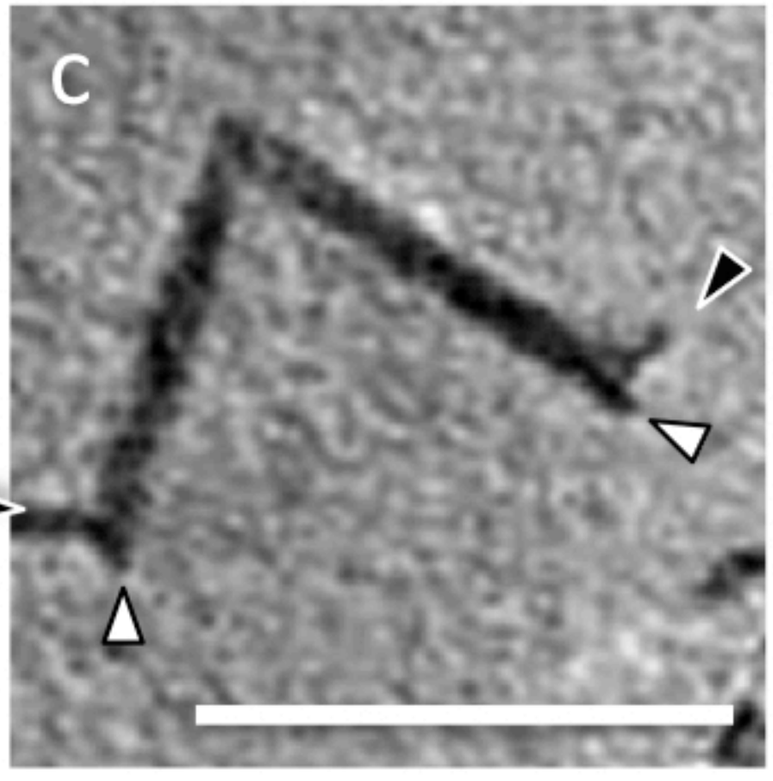
c

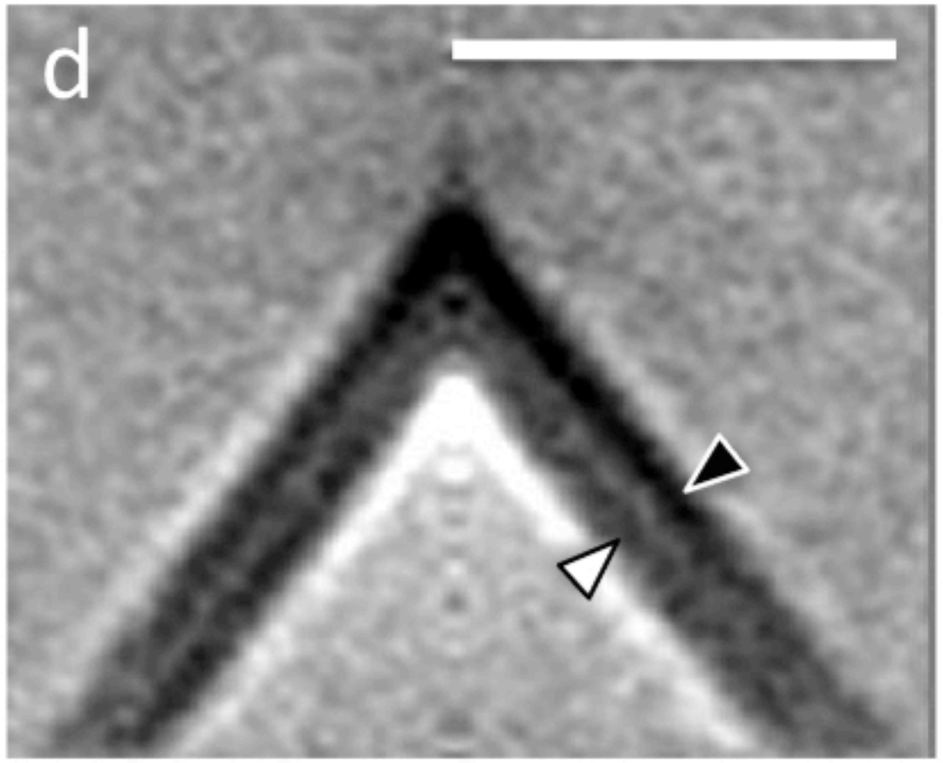
d

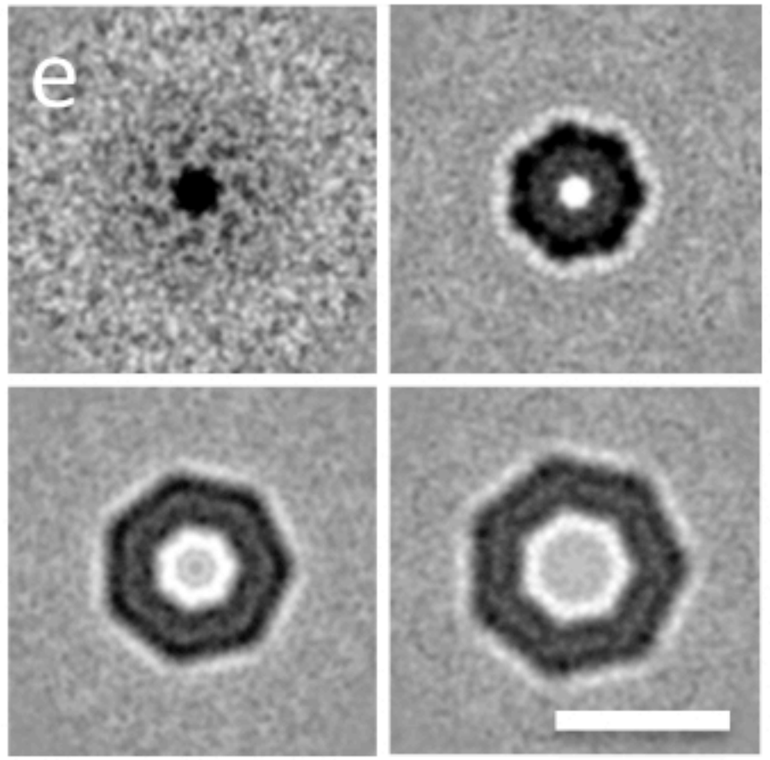
e

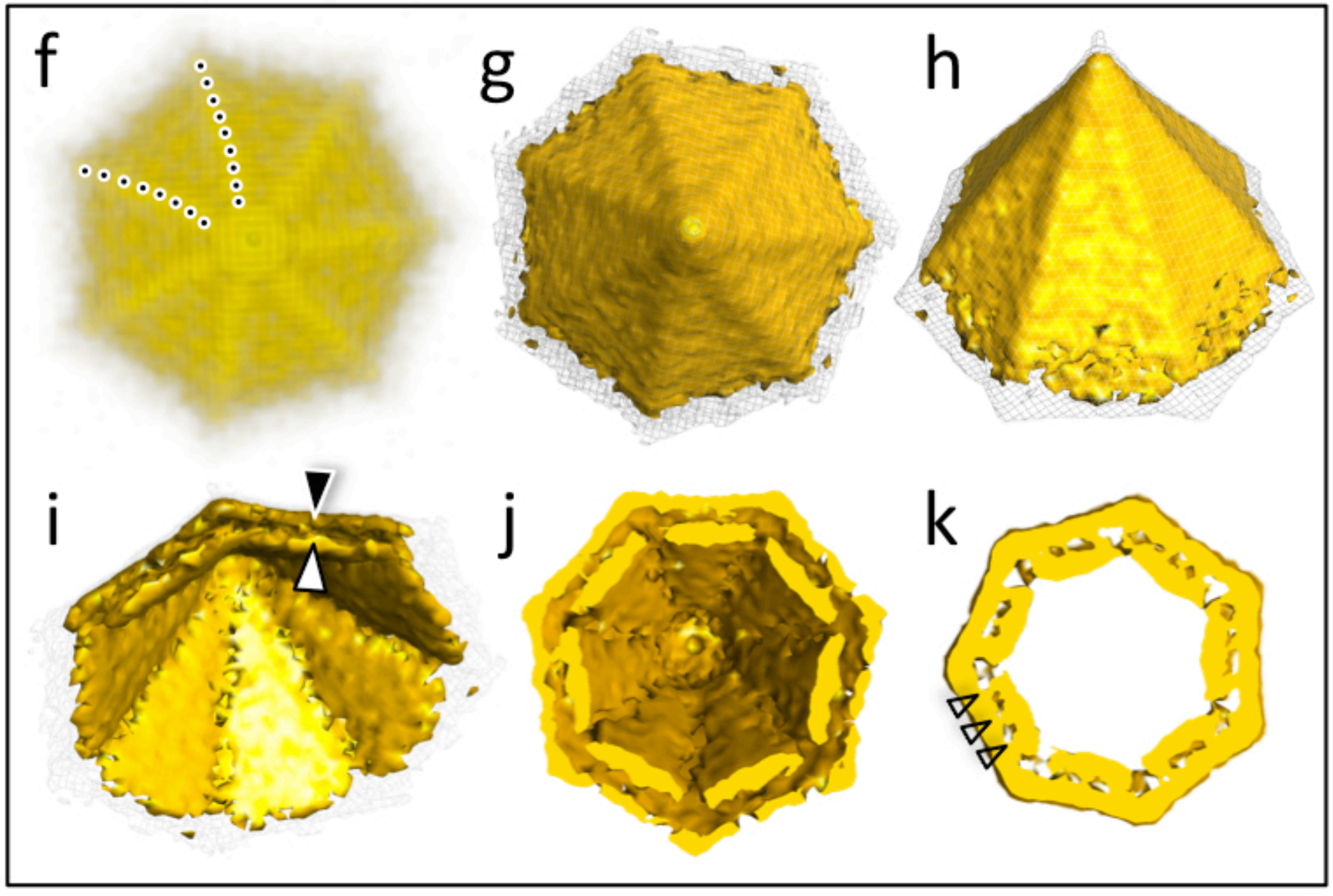
f
g
h
i
j
k

a

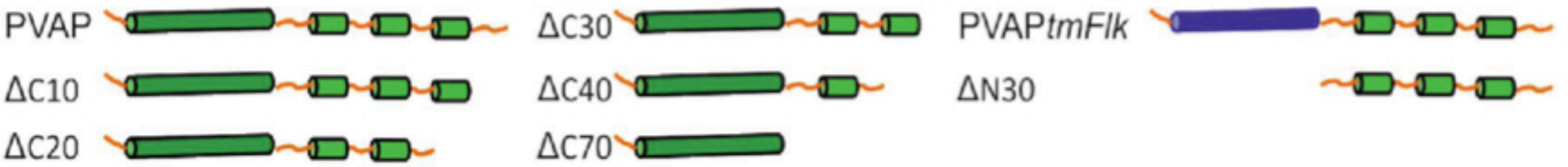
PVAP
ΔC10
ΔC20
ΔC30
ΔC40
ΔC70
PVAP*tmFlk*
ΔN30

b

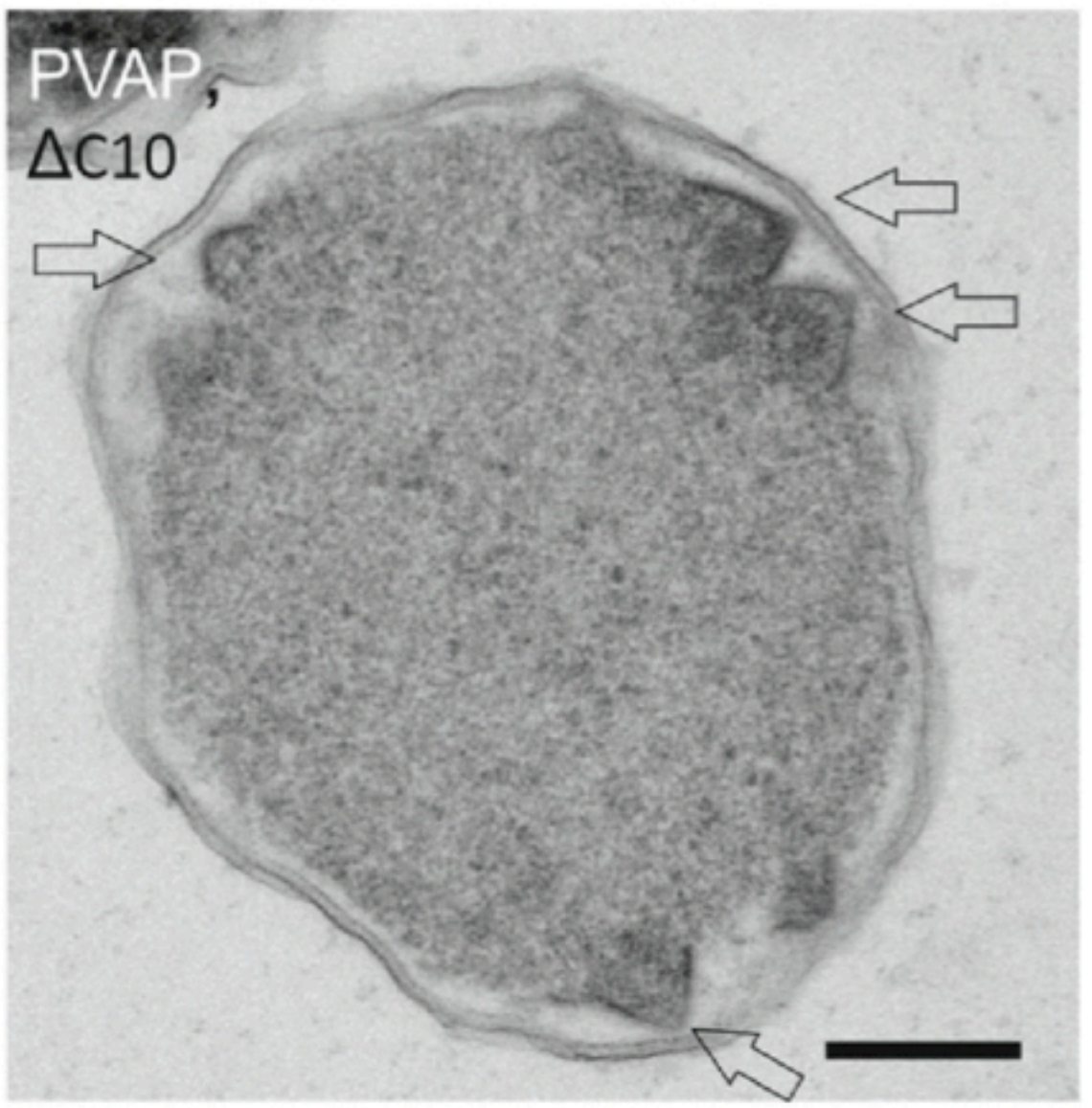
PVAP,
ΔC10

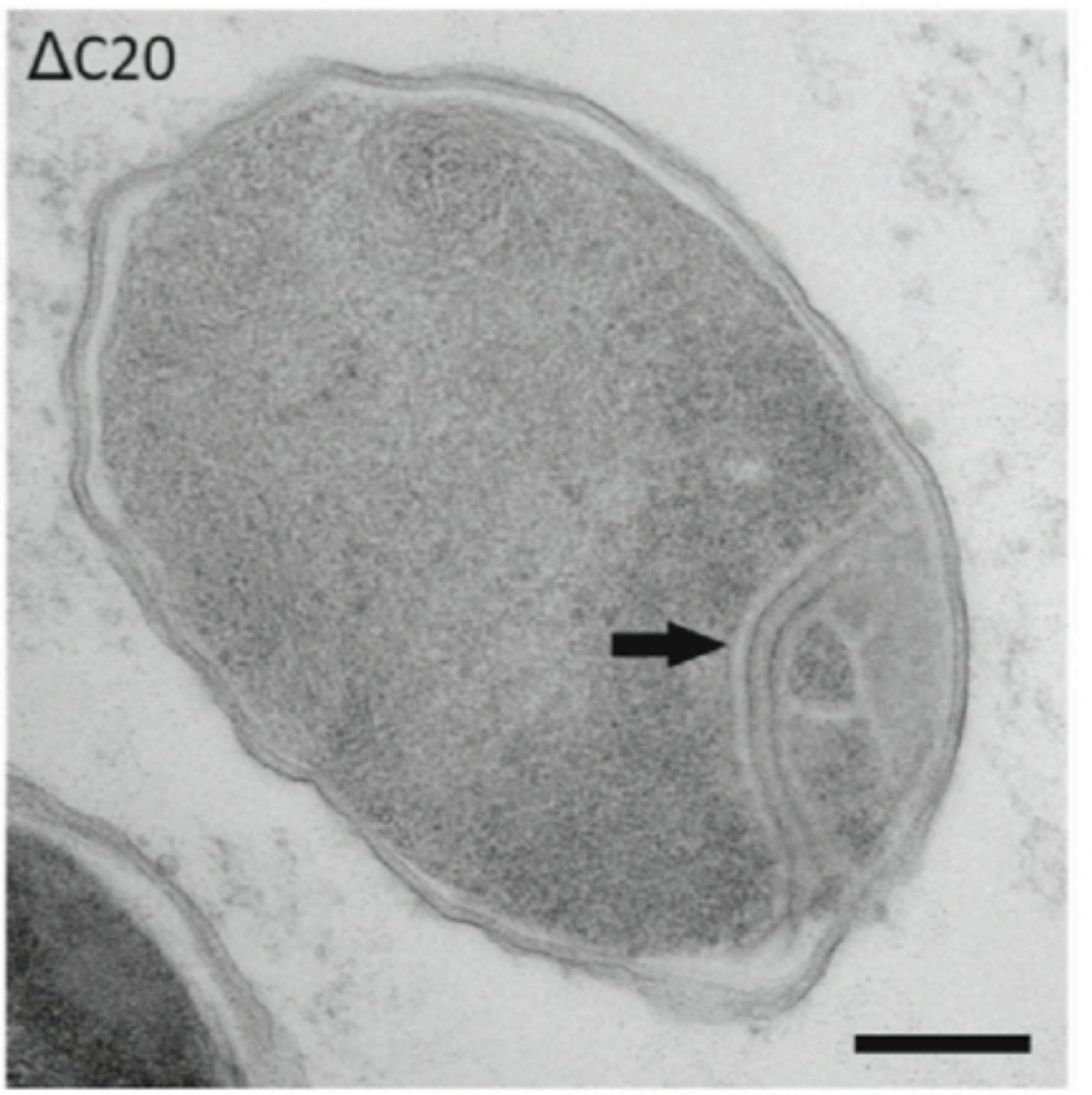
ΔC20

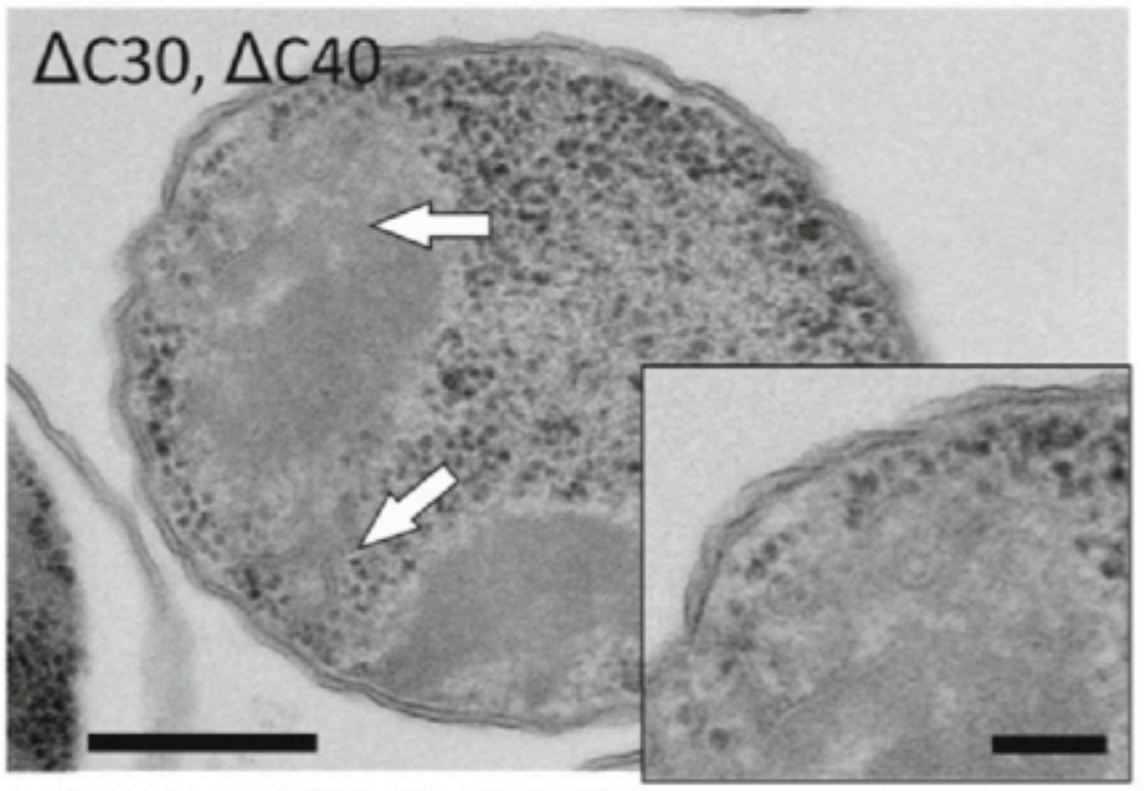
ΔC30, ΔC40

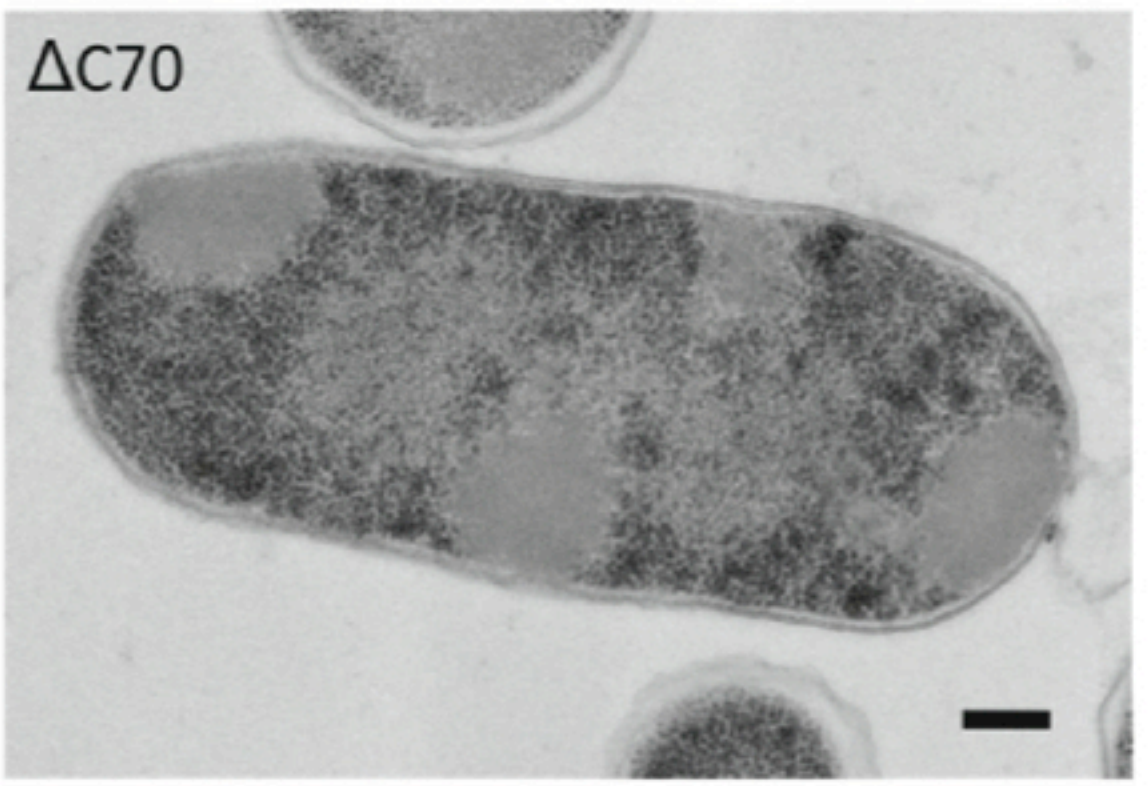
ΔC70

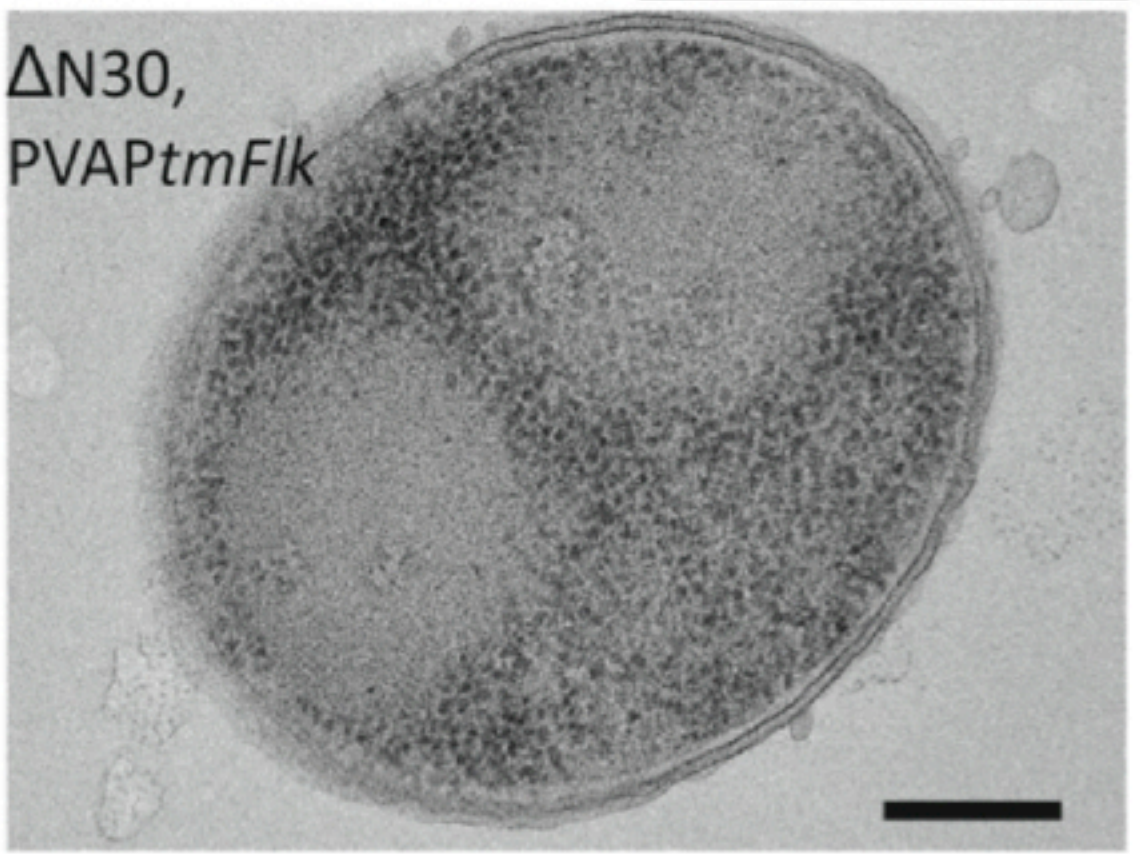
ΔN30,
PVAP*tmFlk*

a

PVAP

N

TM

outside

C

cytoplasm

c

b

cytoplasm

Supplementary Figure Legends

Supplementary Figure 1. Early stage of VAP assembly. Consecutive tomographic slices through nascent VAP at 3 h.p.i. in *S. islandicus* host cell. Black arrows indicate VAP. PM, plasma membrane. Scale bar: 100 nm

Supplementary Figure 2. Secondary structure prediction of PVAP. Sequence of wild type PVAP (black lettering) with predicted secondary structure as indicated. Blue, predicted α-helices (a); yellow, coils (c); red, strands (e). TM segment, predicted trans-membrane segment.

Supplementary Figure 3. VAPs in *E. coli* and *S. acidocaldarius*. Tomographic slices trough *E. coli* (upper panel) and *S. acidocaldarius* (lower panel) cells expressing PVAP. VAPs in *E.coli* remain closed for longer than 2 weeks. VAPs in *S. acidocaldarius* open ~72 hours after PVAP induction; bars, 500 nm.

Supplementary Figure 4. Unsymmetrised subtomogram average of VAPs. Average of 57 VAPs obtained from *E. coli* cells overexpressing PVAP. Slices run perpendicular (a) or parallel (b) to the base of the pyramid. The unsymmetrized average shows clear 7-fold symmetry around an axis perpendicular to the base. Scale bars: 50 nm.

Supplementary Figure 5. Resolution estimate of VAP subtomogram average. (a) Local resolution for successive slices through the 3D map is shown in different colours. **(b)** Histogram showing the number of voxels for which a certain resolution was estimated. The estimated local resolution of the average is between 36 and 58 Å. Mean and median resolution are 43 and 42 Å, respectively.

Supplementary Figure 6. Flk-PVAP fusion protein localizes to *E.coli* membranes. SDS/PAGE of: 1, marker; 2, SIRV2-infected *S. islandicus*, 10 hpi; 3-4, membrane fraction of *E. coli* expressing Flk-PVAP fusion (PVAP*tmFlk*); 5-6 cytosolic fraction of *E.coli* expressing PVAP*tmFlk*. The *E. coli* samples were loaded undiluted or diluted 1:10. The positions of proteins with known molecular mass (in kDa) are indicated by bars based on the marker loaded in the first lane. (a) Coomassie Blue–stained gel. (b) Western blot of a duplicate gel with antibodies against SIRV2-PVAP. Mem, membrane fraction; Cyt, cytosolic fraction

Supplementary Figure 7. Analytical size exclusion chromatography of PVAP. Elution profile of PVAP on the Superdex75 column shows a symmetrical peak eluting at 70 kDa. SDS-PAGE of the peak fraction and Western-Blot analysis with antibodies against PVAP indicate protein bands at the level expected for the PVAP monomer, dimer, trimer and heptamer.

Supplementary Movie 1. 3D map of the VAP. Subtomogram average of **57** VAPs in closed state.

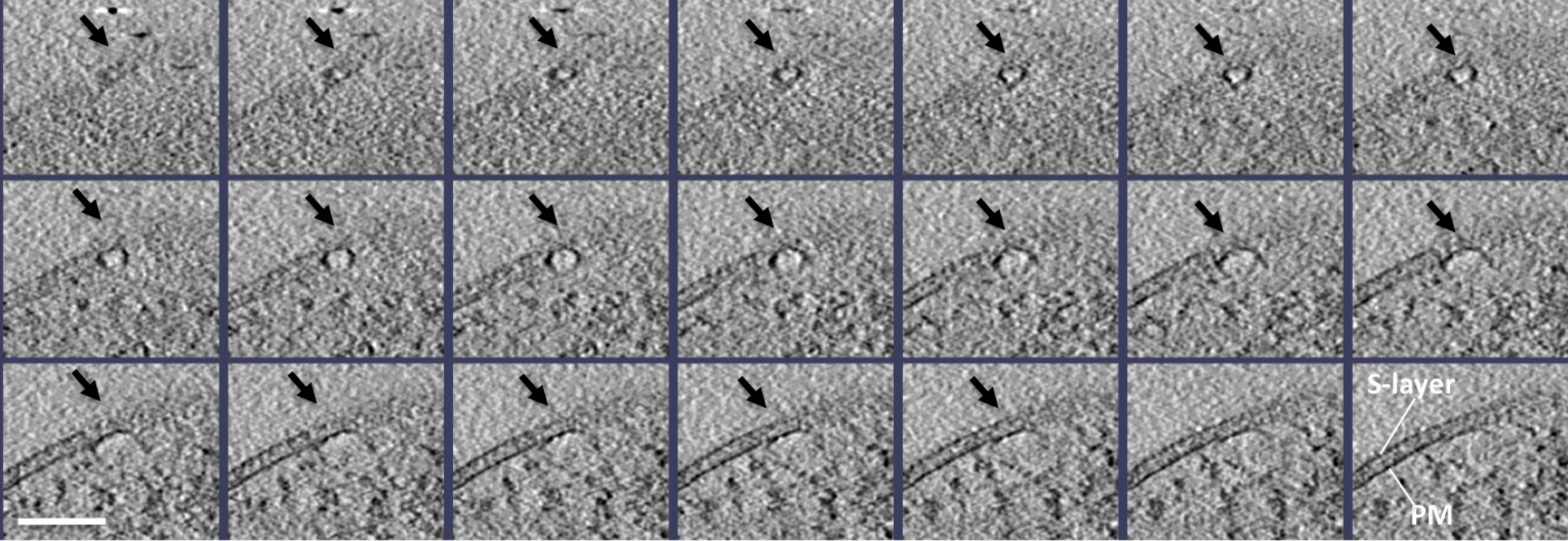
S-layer
PM

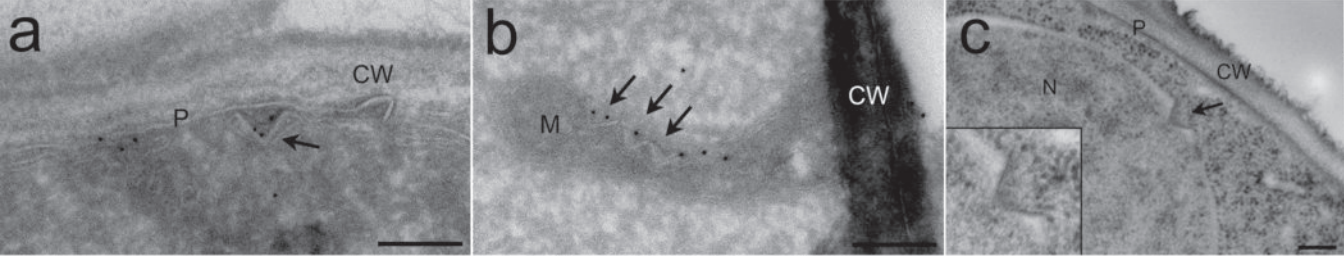
a
CW
P
b
M
CW
c
P
N
CW

Supplementary Methods

Virus and host strains The SIRV2 virus stock was prepared and the *S. islandicus* LAL 14/1 strain grown as described previously (1). For analysis of morphological changes upon viral infection, cells were synchronized by dilution of precultures in fresh medium. The cultures were grown for ~12 hours until an OD of 0.1-0.2 was reached and SIRV2 was added directly to the cultures as described (1).

Plasmid constructs and transformation of *S. acidocaldarius* For the expression of *PVAP* in *S. acidocaldarius* M31, SIRV2_ORF98 (NCBI RefSeq ID: NP_666583) was amplified from SIRV2 genomic DNA and cloned into the lacS gene locus in the pMZ1 plasmid (2) using the NcoI and BamHI sites. SIRV2_ORF98 (PVAP) and the araS promoter were transferred from pMZ1 to the pSVA1450 plasmid (3) using the NcoI and EagI sites, which yielded pTQ26. pTQ26 was transformed to *S. acidocaldarius* M31. The preparation of competent cells, methylation of the plasmid, and electroporation were carried out as described (4) using a Bio-Rad Gene Pulser Xcell electroplater with 1-mm cuvettes at 1,500 V, 600 Ω, and 25 μF. Selection of *PVAP* expressing colonies and induction of expression were performed as before (5).

Plasmid constructs and transformation of *E.coli* For the overexpression of *SIRV2_ORF98* (*PVAP*) C-terminal truncation mutants in *E. coli* Rosetta(DE3)pLys (Novagen Merck), SIRV2_ORF98 was amplified from SIRV2 genomic DNA with different reverse primers resulting in PCR products of 297 (full length), 267 (-10 AA), 237 (-20 AA), 207 (-30 AA), 177 (-40 AA), 87 (-70 AA) bp. PCR amplification of a 216 bp product starting 81 bp downstream of the ATG resulted in a PVAP mutant lacking the N-terminal transmembrane domain. The same sequence was used for a fusion with the 75 bp transmembrane segment of the *E.coli Flk* gene, preceded by the 27 N-terminal bp of PVAP. This oligonucleotide sequence was synthesized by GeneArt® (Invitrogen). All *PVAP* gene mutants were cloned into the T7 promoter–driven expression vector pSA4 using the NcoI and BamHI sites (6). The pSA4 vector contains an isopropyl β-d-1-thiogalactopyranoside–inducible promoter that was used for the expression of a C-terminally His-tagged protein. Analysis of *PVAP* expression cultures by high pressure freezing and freeze substitution was performed as described (5). The location of the Flk-PVAP fusion was analyzed by isolation of membranes as described in ref (11), followed by SDS PAGE, western blotting and immunolabelling with antibodies raised against PVAP as described (5).

Plasmid constructs and transformation of *S. cerevisiae* For the overexpression of *SIRV2_PVAP* (*PVAP*) in *Saccharomyces cerivisiae, SIRV2_PVAP* was amplified from SIRV2 genomic

DNA and cloned in the expression vector pCM190 (7) using PstI and XbaI sites. *S. cerivisiae* was transformed with the plasmid according to Gari et al. (7). After selection on plates without uracil a single colony was picked and grown at 30 °C overnight in a pre-culture in selective uracil-free medium, and with 10 microgram/ml doxycyclin. After one day, cells were diluted 1/1000 in medium without doxycyclin.

Immuno-electron microscopy Yeast cells were fixed with 4% paraformaldehyde in 0.1M Hepes, pH 5.4 for 2 h at RT. The cells were then washed with 50 mM NH_4Cl in PBS to quench free aldehyde groups and pelleted in 12% gelatin in PBS. The gelatine pellet was solidifed on ice and cut into small blocks, which were infiltrated over night at 4°C with 2.3M sucrose for cryoprotection, mounted on aluminium pins and frozen in liquid nitrogen. Thin sections were cut with a UC6/FC6 (Leica microsystems, Vienna, Austria) and picked up in a 1:1 mixture of 2.3M sucrose and 2% methylcellulose (8). Labelling for PVAP was done as described previously (5).

High-pressure freezing and freeze-substitution *E.coli* cells were taken up in cellulose capillary tubes (Leica Microsystems GmbH, Vienna, Austria) as described in (9). *S. cerevisiae* cultures were concentrated by filtration. Tubes or cell concentrates were placed into brass planchettes filled with 1-hexadecen (Agar Scientific, Stansted, United Kingdom). Samples were frozen in a HPM 010 high pressure freezer (Baltec, now Abra Fluid AG, Widnau, Switzerland). Freeze-substitution was performed in anhydrous acetone containing 2% osmium tetroxide (Merck, Germany). Small cracks were introduced under liquid nitrogen in solid 1-hexadecen by pre-cooled fine point forceps (No 5, Dumont, Switzerland) to allow perfusion of the substitution mix. Freeze-substitution was carried out at -90°C for 24h, and at -60°C and -30°C for 8h each in a freeze substitution device (Leica Microsystems GmbH, Vienna, Austria). Afterwards the temperature was raised to 0°C and the samples were washed with dry acetone and embedded stepwise in EPON. After heat polymerization thin sections were cut with an Ultracut UCT microtome (Leica Microsystems GmbH, Vienna, Austria). Sections were collected on 200 mesh Formvar-coated copper grids and post-stained with 4% uranylacetate and Reynold's lead citrate. Images were recorded with a JEOL 1010 electron microscope at 80 kV equipped with an Olympus Keen View camera (Olympus Soft imaging systems, Münster, Germany).

Whole cell cryo-tomography *S. islandicus* cells were harvested shortly after infection, concentrated by low-speed centrifugation (3000 rpm for 10 min) and plunge-frozen directly in the growth medium. For this, cell pellets were resuspended in an equal volume of fresh medium. *E. coli* cells overexpressing *PVAP* were harvested at the same conditions, washed once in 50mM Tris, 300mM NaCl, pH7 and plunge-frozen in the same buffer. Before freezing, suspensions were

mixed with an equal volume of 10 nm colloidal protein-A gold suspension (Aurion, Wageningen, The Netherlands). 3 µl of this mixture were added to a 300 mesh R2/2 glow-discharged Quantifoil grid, blotted and rapidly injected into liquid ethane using a homemade plunge freezer. Tomograms were recorded with a Polara G2 Tecnai field emission transmission electron microscope (FEI, Hillsboro, USA) operated at 300 kV, equipped with a Gatan Tridiem energy filter and 2x2 k CCD camera (Gatan Inc., Pleasanton, USA). Zero-loss filtered images were collected using the Digital Micrograph software (Gatan Inc., Pleasanton, USA). Tomographic tilt series were recorded with the FEI tomography software (FEI Company, Hillsboro, USA). Tilt series were generally collected in a range of -60° to +60° in steps of 1.5° or 2°, at 6-9 µm defocus and magnifications of 41.000x, 34.000x or 27.500x, corresponding to a pixel size of 0.5766nm, 0.709nm or 1.073nm, respectively. Tomograms were reconstructed using the IMOD software package (10) and de-noised by non-linear anisotropic diffusion (NAD) (11).

Subtomogram averaging For subtomogram averaging of VAPs, 57 pyramid volumes were cut out from a single tomogram of a PVAP overexpressing *E. coli* cell, aligned and averaged using the PEET software (12,13) as described before (14). The average volumes were averaged further by applying 7-fold rotational symmetry. 3D maps obtained by subtomogram averaging were displayed and analyzed in 3Dmod (IMOD,(34)) or UCSF chimera (15). The resolution of the map was estimated using the ResMap software (16).

PVAP purification The codon-optimized gene coding for PVAP was synthetized (Genscript) and inserted in to the expression plasmid pET26b (Novagene) using the restriction sites NdeI and XhoI. *E. coli* BL21DE3/Rosetta/pLysS cells were transformed with the resulting plasmid and transformants were selected using kanamycin (Kan, 50µg/ml) and chloramphenicol (Cam, 34µg/ml). An overnight pre-culture of a single colony was transferred to 12L “terrific broth” (TB) medium containing Kan and Cam and incubated in the shaker at 160 rpm until the optical density at 600nm (OD_{600}) reached 0.8 - 1.0. Protein expression was induced with 1mM IPTG (isopropyl-β-D-1-thio-galacatopyranoside) at 37°C. After 2 hours, cells were pelleted, resuspended in lysis buffer (50 mM Tris pH 7.0, 300 mM NaCl, 0.5 mM PMSF) and disrupted with a Microfluidizer (M-110L, Microfluidics Corp., Newton, MA). Unbroken cells were removed by 30 min. centrifugation at 14,000g. The membrane fraction was pelleted by centrifugation of the supernatant at 100.000g for 90 min. at 4°C ,resuspended in 50 mM Tris pH 7.0, 300 mM NaCl and diluted to a protein concentration of 5 mg/ml. Membranes were solubilized by adding of N-laurylsarcosine to a final concentration of 1.5%. Non-solubilized protein was removed by centrifugation for 60 minutes at 100.000g. The supernatant containing the His-tagged protein was loaded onto a Ni-NTA column and unspecifically bound proteins were removed in several

washing steps. The protein was eluted in buffer containing 500 mM imidazole and concentrated using Amicon spin columns (Millipore) with a 30 kDa cutoff prior to loading onto a gel filtration column (Superdex75). Purified protein was eluted using 50 mM Tris pH 7.0, 300 mM NaCl and 0.05 % N-laurylsarcosine as running buffer.

References

1. Bize A*, et al.* (2009) A unique virus release mechanism in the Archaea. *Proc Natl Acad Sci U S A* 106(27):11306-11311.

2. Zolghadr B, Weber S, Szabo Z, Driessen AJ, & Albers SV (2007) Identification of a system required for the functional surface localization of sugar binding proteins with class III signal peptides in Sulfolobus solfataricus. Mol Microbiol 64(3):795-806.

3. Wagner M, et al. (2013) Investigation of the malE promoter and MalR, a positive regulator of the maltose regulon, for the vector system in Sulfolobus acidocaldarius. Appl Environ Microbiol doi: 10.1128/AEM.03050-13.

4. Berkner S & Lipps G (2007) Characterization of the transcriptional activity of the cryptic plasmid pRN1 from Sulfolobus islandicus REN1H1 and regulation of its replication operon. J Bacteriol 189(5):1711-1721.

5. Quax TE*, et al.* (2011) Simple and elegant design of a virion egress structure in Archaea. *Proc Natl Acad Sci U S A* 108(8):3354-3359.

6. Albers SV, Szabo Z, & Driessen AJ (2003) Archaeal homolog of bacterial type IV prepilin signal peptidases with broad substrate specificity. J Bacteriol 185(13):3918-3925.

7. Gari E, Piedrafita L, Aldea M, & Herrero E (1997) A set of vectors with a tetracycline regulatable promoter system for modulated gene expression in Saccharomyces cerevisiae. Yeast 13(9):837-848.

8. Liou W, Geuze HJ, & Slot JW (1996) Improving structural integrity of cryosections for immunogold labeling. Histochem Cell Biol 106(1):41-58.

9. Hohenberg H, Mannweiler K, & Müller M (1994) High-pressure freezing of cell suspensions in cellulose capillary tubes. J Microsc 175(Pt 1):34-43.

10. Kremer JR, Mastronarde DN, & McIntosh JR (1996) Computer visualization of three-dimensional image data using IMOD. J Struct Biol 116(1):71-76.

11. Frangakis AS & Hegerl R (2001) Noise reduction in electron tomographic reconstructions using nonlinear anisotropic diffusion. J Struct Biol 135(3):239-250.

12. Nicastro D (2009) Cryo-electron microscope tomography to study axonemal organization. Meth Cell Biol 91:1-39.

13. Nicastro D , et al.(2006) The molecular architecture of axonemes revealed by cryoelectron tomography. Science 313(5789):944-948.

14. Davies KM, Anselmi C, Wittig I, Faraldo-Gomez JD, & Kühlbrandt W (2012) Structure of the yeast F1Fo-ATP synthase dimer and its role in shaping the mitochondrial cristae. Proc Natl Acad Sci USA 109(34):13602-13607.

15. Pettersen EF, et al. (2004) UCSF chimera - A visualization system for exploratory research and analysis. J Comput Chem 25(13):1605-1612.

16. Kucukelbir A, Sigworth FJ, & Tagare HD (2013) Quantifying the local resolution of cryo-EM density maps. *Nature meth*. doi: 10.1038/nmeth.2727.